ACS APPLIED MATERIALS & INTERFACES

www.acsami.org

Research Article

Rapid Synthesis of Nanoporous Zn Powder by Selective Etching of Al from Micrometer-Sized Zn−Al Powder Particles Produced by Gas Atomization and Its Application in Hydrogen Generation

Jo Kubota, Jiaxin Liu, and Eric Detsi*

Cite This: ACS Appl. Mater. Interfaces 2024, 16, 70469−70476

Read Online

ACCESS | Metrics & More | Article Recommendations | Supporting Information

ABSTRACT: The scalable synthesis of non-precious nanoporous metals, such as nanoporous zinc (NP-Zn), nanoporous iron (NP-Fe), and nanoporous aluminum (NP-Al), is crucial for large-scale production of hydrogen through the reaction between non-precious metals and water. The fabrication of bulk NP-Zn by selective removal of Al from sub-centimeter-sized arc-melted Zn−Al parent alloys through free corrosion dealloying usually takes a few days. Here, we demonstrate that this free corrosion dealloying process can be reduced from a few days to 4 min simply using micrometer-sized Zn−Al powder particles with nominal composition $Zn_{40}Al_{60}$ atomic % produced by gas atomization as the parent alloy. Reducing the size of the parent alloy significantly enhances the dealloying rate. Furthermore, Al and Zn are phase-separated in Zn−Al powder particles due to the gas atomization process, making removing the sacrificial Al phase easy. We used various techniques, including X-ray diffraction, Xe^+ plasma focused ion beam/scanning electron microscopy (FIB/SEM), energy-dispersive spectroscopy (EDS), and inductively coupled plasma optical emission spectroscopy (ICP−OES) to thoroughly characterize these materials before and after free corrosion dealloying. The fabricated NP-Zn powder exhibits a hierarchical ligament/pore morphology, with tiny structures with a size of ≈10 nm coming from Zn nanoparticle aggregation during dealloying and large structures in the range of ≈50−200 nm coming from the removal of the sacrificial Al phase. We demonstrate that this NP-Zn can spontaneously react with water at near-neutral pH to produce hydrogen and zinc oxide solid byproducts with a hydrogen generation yield of ≈52% within 60 min.

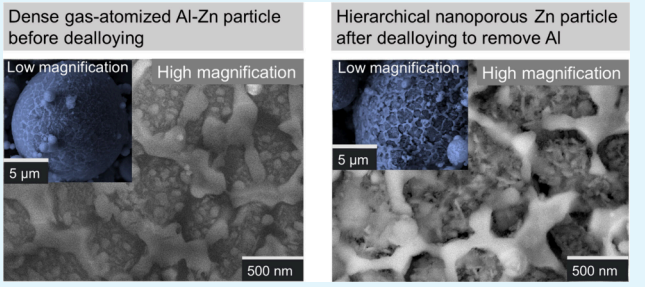

KEYWORDS: *dealloying, nanoporous zinc, metal−water reaction, hydrogen generation, focused ion beam milling and imaging*

1. INTRODUCTION

Due to their high surface-area-to-volume ratio and ample catalytically active sites, such as specific facets, steps, and kinks, dealloyed nanoporous metals are desirable for various applications, such as electrocatalysis,[1,2] energy conversion and storage,[3,4] actuation,[5,6] plasmonics,[7,8] and structural application.[9,10] In particular, bulk nanoporous metals offer the benefits of bulk metals, including handleability, mechanical integrity, and thermal and electrical conductivity, as well as the benefit of nanostructured materials, such as size-dependent properties,[11] low density,[12] and high catalytic activity.[13,14] In most chemical and electrochemical applications of nanoporous metals, significant focus has been directed toward precious metals, such as nanoporous Pt,[15] Pd,[16] Ag,[17] and Au.[18] This is primarily because the relatively low chemical reactivity of the precious metals makes it easy to fabricate them in a nanoporous format and characterize them. Further, most precious metals are great catalysts as they lower the activation energy barrier and increase the kinetics of the desired reactions.[19] However, the relatively high cost and scarcity of the precious metals hinder their use in large-scale applications, including hydrogen production.[20]

Non-precious metals, which are earth-abundant and more affordable, are more attractive for industrial-scale applications than platinum group metals (PGMs). Although several studies suggested promising applications for non-precious metals, such as Fe, Zn, Al, and Mg,[21−23] non-precious nanoporous metals have seen limited fabrication due to their inherent high chemical reactivity with external environments.[1] Specifically, synthesizing pure, non-precious nanoporous metals is challenging due to their oxygen- and water-sensitive nature. Various reactive nanoporous metals, including nanoporous Al, nanoporous Mg, and nanoporous Zn, have been fabricated in bulk form for on-demand and on-board hydrogen generation via metal−water reactions (metal hydrolysis). For example, Lee et al. fabricated air-stable nanoporous Al/lithium borohydride

Received: August 8, 2024
Revised: November 29, 2024
Accepted: December 2, 2024
Published: December 13, 2024

https://doi.org/10.1021/acsami.4c13394
ACS Appl. Mater. Interfaces 2024, 16, 70469−70476

composite fuel pellets for on-board hydrogen generation.[24] Corsi et al. and Lee et al. synthesized bulk nanoporous aluminum via electrolytic dealloying for on-demand hydrogen generation in neutral water, yielding ≈52%.[25,26] Fu et al. fabricated nanoporous Mg and nanoporous Zn through free-corrosion dealloying for hydrogen generation in neutral water, achieving a yield of ≈22 and ≈16% from Mg and Zn, respectively.[27] These reactive nanoporous metals are monolithic and fabricated as bulk pieces. Due to the limited accessibility to the sacrificial element, the selective etching process is prolonged and the reactivity of the materials remains low. For instance, bulk monolithic NP-Zn requires 3 days to complete its selective etching process, and the hydrogen generation yield is only ≈16% after 500 min of reaction.[27] For large-scale applications, a process that will enable the synthesis of high-performance NP-Zn in a few minutes, as opposed to a few days, is desirable. Therefore, this work aims to introduce an innovative and scalable method for producing NP-Zn in powder form within 4 min instead of 3 days. Furthermore, synthesized NP-Zn can produce hydrogen with a yield of ≈52% within 60 min.

2. EXPERIMENTAL METHODS

2.1. Fabrication of Nanoporous Zinc. A commercial Zn−Al parent alloy in powder form, made by gas atomization, was obtained from Valimet, Inc. The nominal composition and particle size, as provided by the supplier, were $Zn_{40}Al_{60}$ and 1−10 μm, respectively. The Zn−Al alloy powder was used as-received to fabricate NP-Zn by keeping the alloy powder in 1 M NaOH solution for 3, 4, and 5 min to remove Al selectively. The solution was stirred at room temperature on a magnetic stirrer plate for uniform leaching. After Al dissolution, the remaining powder was washed with deionized (DI) water and rinsed with isopropyl alcohol (IPA) for rapid drying. The NP-Zn powder was collected from IPA by vacuum filtration using a Buckner funnel (Fisher) and a Nylon membrane filter with a pore size of 200 nm (Omicron).

2.2. Characterization. We used Xe^+ focused ion beam/scanning electron microscopy (FIB/SEM) to cut through the powder particles before and after dealloying to investigate their microstructure. The elemental compositions of the actual Zn−Al parent alloy and the corresponding dealloyed NP-Zn were analyzed with energy-dispersive spectroscopy (EDS) and inductively coupled plasma [ICP, Spectro Genesis inductively coupled plasma optical emission spectroscopy (ICP−OES) device]. The sample solution for ICP was prepared by dissolving the powders in 0.1 M nitric acid (HNO_3) solution so that the concentrations of the elements are 2−10 ppm, with a standard reference solution (multielement standard solution 5 for ICP, Supelco). The crystal structure of the samples before and after the dealloying was investigated using X-ray diffraction (XRD, Rigaku) with Bragg−Brentano parafocusing geometry operating with a Cu $K\alpha_1$ line at a wavelength of 1.5405 Å and a horizontal goniometer collecting at an angle range from 10° to 90° with a step size of 0.02° and a scanning speed at 5°/min. Before XRD measurement, the powder sample was sealed inside the glovebox with Kapton tape (Ted Pella, Inc.) to minimize air exposure and oxidation. The Zn−Al parent alloy powder and dealloyed NP-Zn samples were stored in an argon environment, with the concentrations of water and oxygen maintained below 0.1 ppm.

2.3. Hydrogen Generation. The water displacement method was used to measure hydrogen produced from the reaction between NP-Zn and water at a near-neutral pH. A three-neck flask was used as the reaction chamber for the hydrolysis reaction, and one of the necks was connected to a graduated cylinder flipped and immersed in water. Evolved hydrogen was collected in the cylinder, and the amount of hydrogen was deduced from the volume change in the cylinder. The second neck was used to introduce near-neutral electrolytes, and the NP-Zn powder was transferred via the third neck of the flask. Both the second and third necks were sealed with glass stoppers during hydrogen production. Vacuum grease and plastic joint clips were applied at all connections to ensure sealings. The flask and electrolyte were preheated to 65 °C in an oil bath to simulate the exothermic behavior during Zn hydrolysis. The details and illustration for the experimental setup will be discussed later. A total of 50 mg of NP-Zn powder reacted with the 20 mL of electrolyte containing 0.01 M NaOH water solution to maintain the pH at 10. The volume change due to hydrogen generation was monitored for 1 h with 10 min intervals to record the volume of hydrogen produced, and the total volume change was normalized by the mass of NP-Zn and its stoichiometric amount of hydrogen produced. Each water displacement test was repeated 3 times to check the consistency, and the average values were plotted for further analysis.

3. RESULTS AND DISCUSSION

3.1. Fabrication of Nanoporous Zinc. The NP-Zn powder was synthesized by free corrosion dealloying. During this process, sacrificial Al is selectively etched away from the parent alloy, which consists of micrometer-sized powder particles of the composition of $Zn_{40}Al_{60}$ atomic %, in 1 M NaOH solution (pH of 14). This alkaline environment facilitates the dissolution of Al, which undergoes an oxidation reaction, as described in eq 1. Concurrently, a hydrogen evolution counter-reaction, a reduction reaction, occurs as detailed in eq 2. The electrons released during the oxidation of aluminum (eq 1) are consumed by the reduction reaction (eq 2), leading to the formation of the NP-Zn powder. This dealloying process removes Al, leaving a porous Zn structure behind.

$$Al(s) + 4OH^-(aq) \rightarrow Al(OH)_4^-(aq) + 3e^- \quad (E^\circ = -2.33\ \text{V versus SHE}) \tag{1}$$

$$2H_2O(l) + 2e^- \rightarrow H_2(g) + 2OH^-(aq) \quad (E^\circ = -0.83\ \text{V versus SHE}) \tag{2}$$

Interestingly, the Pourbaix diagram in Figure 1a shows that, during free corrosion dealloying, besides Al dissolution, Zn should also dissolve in an alkaline solution through the oxidation reaction in eq 3 combined with the reduction counter-reaction in eq 2.

$$Zn(s) + 4OH^-(aq) \rightarrow ZnO_2^{2-}(aq) + 2H_2O(l) + 2e^- \quad (E^\circ = -1.22\ \text{V versus SHE}) \tag{3}$$

In other words, it may seem impossible to selectively remove Al from the Zn−Al parent alloy without dissolving Zn. Fortunately, due to the high difference in the standard reaction potential of Al [E° = −2.33 V versus standard hydrogen electrode (SHE) in an alkaline solution] and Zn (E° = −1.22 V versus SHE in an alkaline solution), a phenomenon known in the corrosion science community as cathodic protection will prevent Zn from dissolving. Indeed, when two dissimilar metals with different standard reduction potentials are in physical contact in a corroding environment (Figure 1b), the metal with the lowest standard reduction potential will dissolve with the counter-reaction taking place on the metal with a higher standard reaction potential. In the case of the Zn−Al alloy, Al will dissolve through eq 1, and the hydrogen evolution counter-reaction in eq 2 will preferentially take place on Zn. Because the counter-reaction in eq 2 is a reduction reaction, it automatically prevents Zn from oxidizing. The dissolution of Zn will commence only after the complete dissolution of all Al.

https://doi.org/10.1021/acsami.4c13394
ACS Appl. Mater. Interfaces 2024, 16, 70469−70476

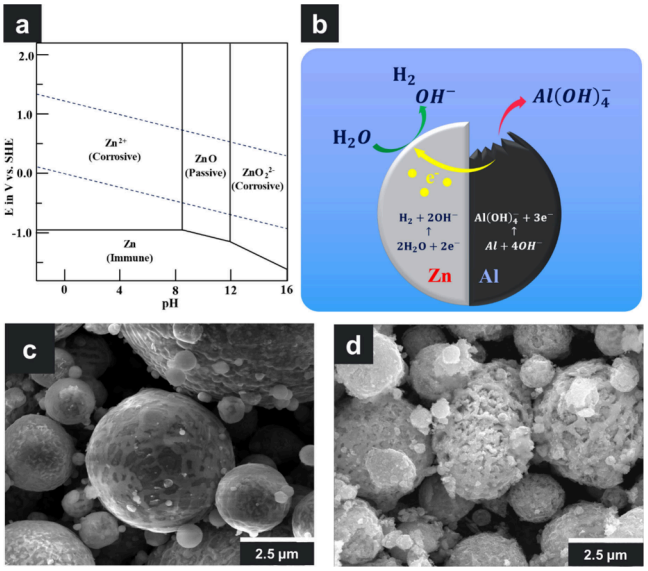

Figure 1. (a) Pourbaix diagram of Zn (adapted with permission from ref 28. Copyright 1951 Electrochemical Society), showing that Zn can dissolve in alkaline when the pH is >12. (b) Simplified free corrosion mechanism of Zn−Al performed in an alkaline corrosive medium. Zn dissolution is prevented by cathodic protection, as Al oxidation provides electrons to Zn and the coupled reduction counter-reaction. (c) SEM image of Zn−Al parent alloy particles consisting of two separated phases: Zn and Al. (d) SEM image of NP-Zn showing the porous structure after dealloying.

In other words, the samples should not be kept in the corroding medium for a long time; otherwise, Zn will dissolve after Al removal. Therefore, we kept the samples in the corrosion medium for 3, 4, and 5 min to identify the optimal dealloying time using XRD analysis. The SEM images in panels c and d of Figure 1 show the typical microstructure of the powder particles before and after dealloying, respectively. The presence of two phases, a Zn-rich phase and an Al-rich phase, in the starting Zn−Al parent alloy powder is confirmed by the contrast from the SEM image of Figure 1c. This contrast originates from the difference in the mass and density of the two phases, as the heavier and more dense Zn-rich phase deflects electrons more strongly, thus appearing to be lighter. In contrast, the less dense Al-rich phase absorbs more electrons, thus appearing darker (Figure 1c). The NP-Zn powder particles in Figure 1d show that the particle shapes are conserved after leaching the sacrificial phase from the parent alloy, and the dealloying process successfully creates porous powder particles from dense particles.

Figure 2 shows four different XRD patterns for the pristine Zn−Al parent alloy (black) and the corresponding samples after 3 min (red), 4 min (green), and 5 min (orange) of free corrosion dealloying. The pristine alloy powder is a mixture of Al and Zn phases, indicated by the coexistence of both Al and Zn XRD patterns in the black curve in Figure 2. Upon dealloying of the parent alloy powder for 3 min, the red XRD pattern in Figure 2 indicates that the resulting product powder is predominantly composed of pure Zn. Additionally, minor peaks at 38.5° and 44.8° correspond to characteristic Al peaks, as highlighted with inverse triangles (▼). These minor peaks suggest the presence of the Al phase, indicating that the dealloying process is not fully complete in 3 min.[17] Although the 3 min dealloyed NP-Zn requires additional leaching, keeping this sample in the corroding medium for 2 min more

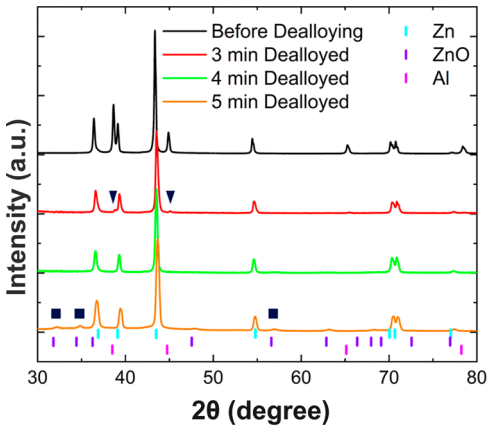

Figure 2. XRD patterns of the Zn−Al parent alloy before dealloying and NP-Zn after dealloying for 3 min (red), 4 min (green), and 5 min (black). NP-Zn dealloyed for 4 min exhibits pure Zn patterns lacking Al and ZnO reflections. NP-Zn dealloyed for 3 min still contains residual Al, as highlighted with inverse triangles (▼), and Zn starts to oxidize after 5 min of dealloying, forming ZnO on the surface, as highlighted with squares (■).

(i.e., from 3 to 5 min) leads to the formation of ZnO, as shown by the orange XRD pattern of the 5 min dealloyed sample in Figure 2, which shows that the product powder is mostly metallic Zn after dealloying for 5 min; however, minor peaks of ZnO highlighted with squares (■) are observed, suggesting that Zn has started to oxidize when Al removal is completed. The optimal dealloying time for the Zn−Al parent alloy powder is determined to be 4 min, as shown in the green XRD pattern in Figure 2, where it can be seen that NP-Zn powder leached for 4 min has neither Al nor ZnO.

In addition to the XRD analysis, we also confirmed the removal of Al using EDS and ICP. EDS was performed on particle cross-sections to determine the composition using FIB/SEM. As shown in Table 1, after 4 min of selective

Table 1. EDS and ICP-Based Elemental Analysis of Zn−Al Powder before and after Dealloying

		Al (atomic %)	Zn (atomic %)
before dealloying	ICP	65.9	34.1
	EDS	51	49
after dealloying	ICP	6.0	94.0
	EDS	1	99

etching, 99% of the product powder consists of Zn (from EDS), indicating that nearly all Al has been successfully removed in the NaOH solution. EDS also suggests that the Zn−Al parent alloy (nominal composition $Zn_{40}Al_{60}$) consists of 51 atom % Al and 49 atomic % Zn. Because our EDS data give the composition within a powder particle, we attribute this 9 atomic % deviation from the nominal composition to the fluctuation in composition among different powder particles. In other words, this deviation would be less if we take the average composition of many powder particles (interparticle composition) instead of within one single particle (intra-particle composition). This motivated us to run ICP to investigate the sample composition more accurately because ICP can give the average composition of a large amount of powder dissolved in acid. The results from Table 1 demonstrate that the overall chemical composition from ICP

https://doi.org/10.1021/acsami.4c13394
ACS Appl. Mater. Interfaces 2024, 16, 70469−70476

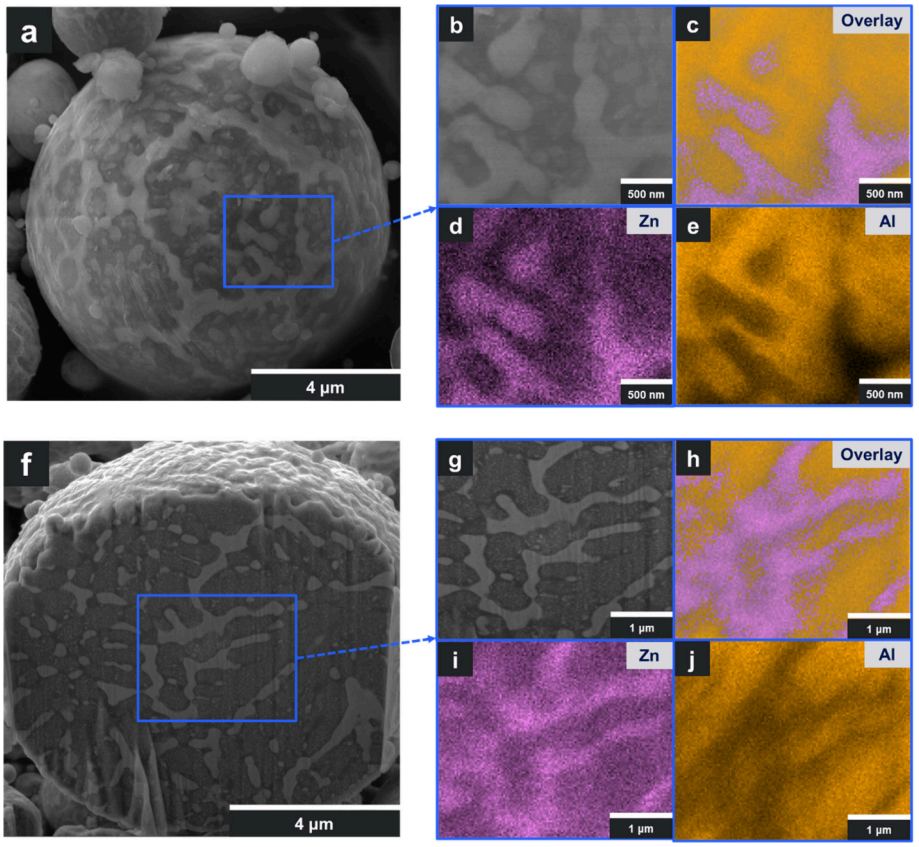

Figure 3. SEM images with corresponding EDS maps of the (a–e) surface and (f–j) cross-section of the Zn–Al parent alloy. (a and f) Low-magnification SEM images illustrating the separation of two phases. (b and g) High-magnification SEM images demonstrating small particles of Zn within the Al phase. The corresponding EDS maps show (c and h) Zn (pink) and Al (orange) overlay, (i) Zn in pink, and (j) Al in orange.

of Al and Zn in the parent Zn–Al alloy is 65.9 and 34.1 atomic %, which is closer to the nominal composition of $Zn_{40}Al_{60}$ atomic % than the EDS data. ICP data also suggest that 4 min of dealloying can dissolve most of the Al phase, and the etched powder only has 6 atomic % of Al remaining (Table 1). Both EDS and ICP characterization confirm the successful removal of Al from the Zn–Al alloy quantitatively.

The pristine Zn–Al powder is further investigated using EDS mapping. Panels a and b of Figure 3 illustrate the coexistence of two phases in Zn–Al powder, while the EDS mappings in panels c–e of Figure 3 confirm that the purple regions correspond to Zn and the orange areas correspond to Al; it signifies the phase separation of the Al and Zn phases in the parent alloy powder. This interconnected structure originates from the immiscibility gap of the Zn–Al material system.[29] As the Zn–Al melt cools during gas atomization, the alloy experiences phase separation of the Al and Zn phases. Such phase separation induces solid compositional fluctuation due to the thermodynamically unstable states.[30] It should also be noted that there are small white precipitations in the dark Al regions in panels f and g of Figure 3 (see also the high magnification images used in the graphical abstract). According to the EDS mapping analysis, the white phase corresponds to Zn, indicating that these small precipitates are Zn within the Al matrix. Such a hierarchical structure of Zn creates a unique morphology once the powder is dealloyed.

Following the dealloying process, images obtained through FIB/SEM and transmission electron microscopy (TEM) illustrate a hierarchical nanoporous structure characterized by large ligaments in the range of ≈50–200 nm (Figure 4b) and smaller ligaments with a size of ≈10 nm (Figure 5c). The large nanoporous structures are the remaining Zn phase from the phase-separated Zn–Al parent alloy after the Al phase has been removed. Zn could sustain its morphology, while Al is selectively etched away because the two phases are already separated before the dealloying. Both EDS mappings on the powder surface (Figure 4c) and the cross-section (Figure 4h) confirm the almost complete removal of Al atoms in NP-Zn. Some signals indicate Al in the map in panels e and j of Figure 4. Still, the EDS spectra in Figures S1 and S2 of the Supporting Information show that the intensity corresponding to Al is almost negligible. In Figure 5a, the large ligaments and pores appear as a dark phase due to their thickness, which prevents electron transparency. Conversely, panels b and c of Figure 5 depict the edges of the larger ligaments, which are thin enough to reveal the smaller porous structures (≈10 nm). This observation suggests that the large ligaments are composed of smaller porous features, thereby demonstrating that NP-Zn particles exhibit a hierarchical nanoporous architecture.

It is emphasized that the dealloying time for our NP-Zn powder is significantly much shorter than the previous study with bulk NP-Zn.[27] The bulk alloy took 3 days to remove Al, but this study shows that Zn–Al powder can be dealloyed in 4 min. The dealloying time is reduced because the micrometer-sized Zn–Al parent alloy powder has a higher surface area and phase-separated Al and Zn phases. The micrometer-sized powder offers more surface area for reacting with the alkaline electrolyte than the centimeter-sized alloy chunk, enhancing the reaction kinetics for Al dissolution. Furthermore, unlike the monolithic single-phase bulk alloy used in previous work, our

https://doi.org/10.1021/acsami.4c13394
ACS Appl. Mater. Interfaces 2024, 16, 70469–70476

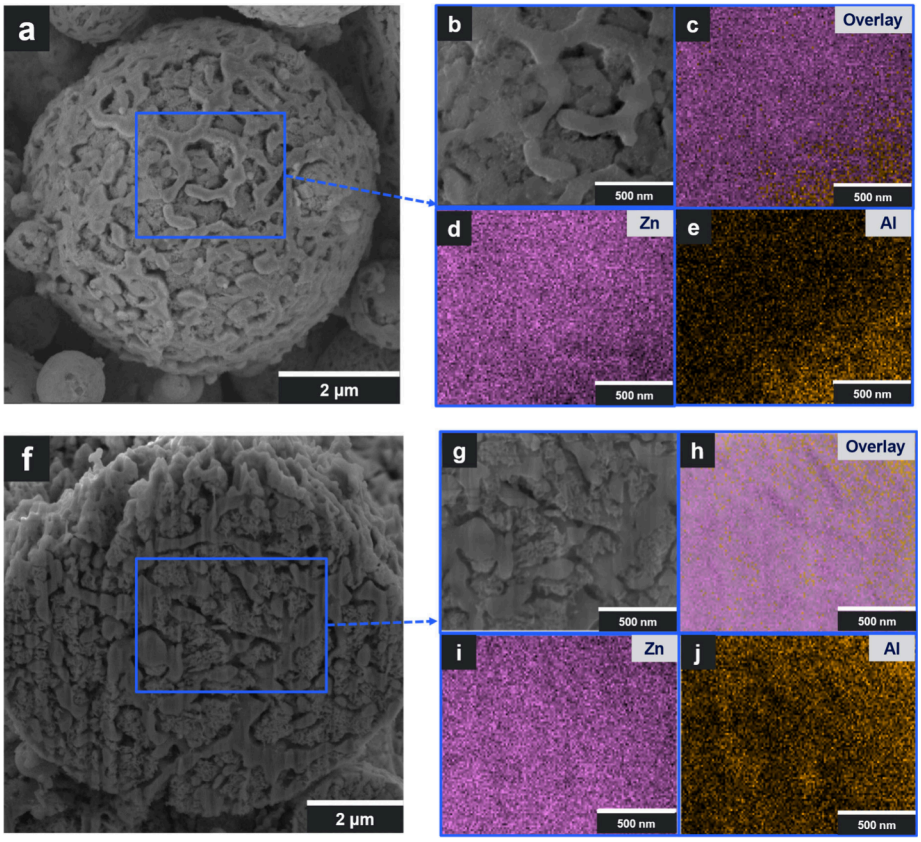

Figure 4. SEM images with corresponding EDS maps of the (a–e) surface and (f–j) cross-section of NP-Zn with a hierarchical nanoporous structure. (a and f) Low-magnification and (b and g) high-magnification SEM images showing the large ligament/pore features in the 100–200 nm range and the small ligament/pore features in the 50–60 nm range. The corresponding EDS maps show (c and h) Zn (pink) and Al (orange) overlay, (d and i) Zn in pink, and (e and j) Al in orange, indicating that NP-Zn consists primarily of Zn.

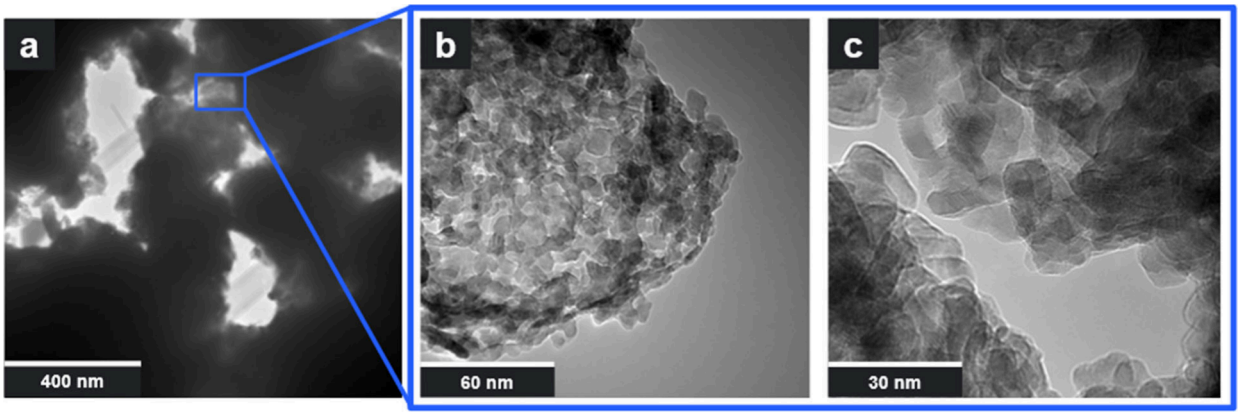

Figure 5. TEM images showing the hierarchical nanoporous structure of NP-Zn at two different magnifications. (a) Low-magnification image shows the large ligament (≈200 nm) observable in the FIB/SEM images. (b and c) Under high magnification, it is found that the large ligaments consist of smaller nanoporous structures with a ligament size of ≈10 nm.

Zn–Al powder contains two distinct regions: Al-rich and Zn-rich regions. With these phases already separated before the dealloying process, Al is more readily removed and dissolved.

3.2. Hydrogen Generation. In this section, we use the setup in Figure 6a to demonstrate that fabricated NP-Zn in the powder form significantly enhances the kinetics of the reaction between Zn and water to produce hydrogen and zinc oxide (ZnO) solid byproduct through eq 4.

$$Zn(s) + H_2O(l) \rightarrow ZnO(s) + H_2(g) \quad (4)$$

In doing so, we compare the yield of hydrogen produced from our NP-Zn powder (black curve in Figure 6b) to that of commercial Zn powder without porosity (red curve in Figure 6b). The primary data of repeated oxidation tests are plotted in Figure S3 of the Supporting Information. After 1 h of reaction, the hydrogen yield for the commercial Zn powder is ≈13%. The hydrogen generation rate significantly slows after 30 min due to forming a passive layer of ZnO (dark blue shell in Figure 7a) around the starting Zn particle. This ZnO shell prevents water from directly contacting metallic Zn underneath

https://doi.org/10.1021/acsami.4c13394
ACS Appl. Mater. Interfaces 2024, 16, 70469–70476

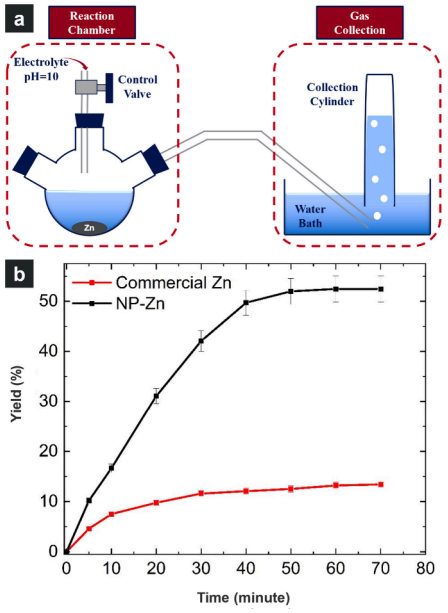

Figure 6. (a) Schematic illustration of the water displacement setup used to measure the hydrogen yield. (b) Hydrogen yield of commercial Zn (red) and NP-Zn (black) as a function of the reaction time. NP-Zn significantly improves the metal−water reaction kinetics due to its nanoporous structure.

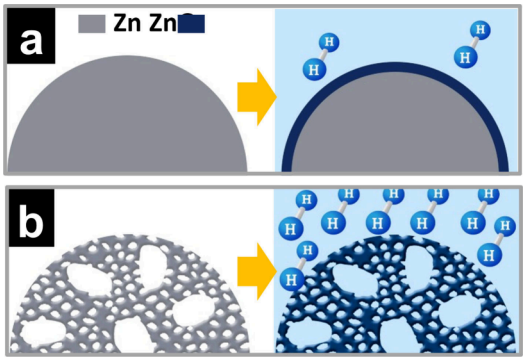

Figure 7. Schematics of the Zn metal−water reaction producing gaseous H_2 and solid ZnO byproduct. (a) Once bulk Zn reacts with water, a layer of ZnO is formed, making the metallic Zn core inaccessible. (b) Zn in NP-Zn can fully react with water due to the porous structure and high surface-area-to-volume ratio, overcoming the issue of the water-blocking oxide layer.

to react further.[27,31,32] On the other hand, a yield of ≈52% is achieved on our NP-Zn within 60 min. The XRD plots in Figure S4 of the Supporting Information also show that oxidation on NP-Zn is more significant than on commercial Zn powder.

This substantial improvement in hydrogen evolution kinetics is attributed to the high surface area and hierarchical porous structure of the NP-Zn powder. The oxidation of Zn is a near-surface reaction, and the extensive surface area provided by the numerous tiny pores, as shown in panels b and c of Figure 5, introduces more reaction sites than commercial Zn dust. While these small pores enhance the metal−electrolyte interface, the larger pores serve as channels that allow the evolved hydrogen gas to escape. This pathway is advantageous for hydrogen evolution because the produced hydrogen gas forms bubbles that can obstruct the surface of metallic Zn, impeding further oxidation.[33] The hierarchical porous structure facilitates the removal of these bubbles, ensuring a continuous and efficient reaction process. The large pores also effectively improve the transport of electrolytes, which can induce more reactions at the inner surface of NP-Zn. We expect further optimization of the dealloying process, and the post-dealloying process can increase the hydrogen production capacity in this material system.

4. CONCLUSION

This study demonstrates the rapid fabrication of NP-Zn by free corrosion dealloying of a commercially available micrometer-sized $Zn_{40}Al_{60}$ parent alloy produced by gas atomization. Prior to this work, the selective etching process to make monolithic bulk NP-Zn typically requires several days. Here, we optimize the dealloying conditions for making NP-Zn in powder form in just 4 min, as opposed to several days. Our expeditious dealloying is enabled through (i) the reduction of the parent alloy size from the centimeter to micrometer range and (ii) the use of the Zn−Al parent alloy in which Al and Zn are already phase-separated. The size reduction in the parent alloy increases the surface area, enabling more sacrificial elements to react with the corroding solution and accelerating the free corrosion dealloying rate. Furthermore, the separation of the Al and Zn phases in the gas-atomized parent alloy enhances Al dissolution. Dealloyed NP-Zn exhibits a hierarchical nanoporous structure with small ligament/pore structures around 10 nm and large ligament/pore structures around 50−200 nm. The large ligament/pore structures correspond to the Zn phase from the phase-separated Zn−Al alloy after the Al phase has been etched away. The small ligament/pore structures result from the agglomeration of Zn nanoparticles, when this Al phase is etched away during dealloying. We also studied how the nanoporous morphology influences the Zn−water reaction, which produces hydrogen and ZnO as the solid byproduct. We found that the dealloyed NP-Zn powder can produce hydrogen from neutral water with a yield of ≈52% within 60 min, while the yield of the conventional dense Zn powder is only ≈13%, demonstrating significant improvement in the reaction kinetics. The hierarchical structure and porous surface facilitate efficient diffusion of the produced hydrogen gas and provide a more accessible metallic surface to react with the solution, respectively. Hydrogen production with NP-Zn through the metal−water reaction is promising for large-scale applications.

■ ASSOCIATED CONTENT

Supporting Information

The Supporting Information is available free of charge at https://pubs.acs.org/doi/10.1021/acsami.4c13394.

EDS spectra of the Zn−Al parent alloy on its surface and cross-section (Figure S1), EDS spectra of NP-Zn on its surface and cross-section (Figure S2), hydrogen yield data of commercial Zn and NP-Zn during the metal−water reaction (Figure S3), and XRD patterns of commercial Zn and NP-Zn after the metal−water reaction (Figure S4) (PDF)

■ AUTHOR INFORMATION

Corresponding Author

Eric Detsi − *Department of Materials Science and Engineering, University of Pennsylvania, Philadelphia, Pennsylvania*

https://doi.org/10.1021/acsami.4c13394
ACS Appl. Mater. Interfaces 2024, 16, 70469−70476

19104, United States; orcid.org/0000-0002-4009-7260; Email: detsi@seas.upenn.edu

Authors

Jo Kubota − *Department of Materials Science and Engineering, University of Pennsylvania, Philadelphia, Pennsylvania 19104, United States;* orcid.org/0009-0008-9843-3416

Jiaxin Liu − *Department of Materials Science and Engineering, University of Pennsylvania, Philadelphia, Pennsylvania 19104, United States;* orcid.org/0009-0005-7001-7945

Complete contact information is available at: https://pubs.acs.org/10.1021/acsami.4c13394

Notes

The authors declare no competing financial interest.

■ ACKNOWLEDGMENTS

The authors gratefully acknowledge the financial support from the National Science Foundation (NSF), Division of Civil, Mechanical, and Manufacturing Innovation (CMMI), NSF CAREER CMMI 2047851 (to Eric Detsi). This work was carried out in part at the Singh Center for Nanotechnology, part of the National Nanotechnology Coordinated Infrastructure (NNCI) Program, which is supported by the NSF Grant NNCI 2025608.

■ REFERENCES

(1) Fu, J.; Welborn, S. S.; Detsi, E. Dealloyed Air- and Water-Sensitive Nanoporous Metals and Metalloids for Emerging Energy Applications. *ACS Appl. Energy Mater.* **2022**, *5* (6), 6516−6544.

(2) Snyder, J.; McCue, I.; Livi, K.; Erlebacher, J. Structure/Processing/Properties Relationships in Nanoporous Nanoparticles As Applied to Catalysis of the Cathodic Oxygen Reduction Reaction. *J. Am. Chem. Soc.* **2012**, *134* (20), 8633−8645.

(3) Zhao, C.; Wada, T.; De Andrade, V.; Gürsoy, D.; Kato, H.; Chen-Wiegart, Y.-c. K. Imaging of 3D Morphological Evolution of Nanoporous Silicon Anode in Lithium Ion Battery by X-Ray Nano-Tomography. *Nano Energy* **2018**, *52*, 381−390.

(4) An, Y.; Fei, H.; Zeng, G.; Ci, L.; Xiong, S.; Feng, J.; Qian, Y. Green, Scalable, and Controllable Fabrication of Nanoporous Silicon from Commercial Alloy Precursors for High-Energy Lithium-Ion Batteries. *ACS Nano* **2018**, *12* (5), 4993−5002.

(5) Jin, H.-J.; Weissmüller, J. Bulk Nanoporous Metal for Actuation. *Adv. Eng. Mater.* **2010**, *12* (8), 714−723.

(6) Biener, J.; Wittstock, A.; Zepeda-Ruiz, L. A.; Biener, M. M.; Zielasek, V.; Kramer, D.; Viswanath, R. N.; Weissmüller, J.; Bäumer, M.; Hamza, A. V. Surface-Chemistry-Driven Actuation in Nanoporous Gold. *Nat. Mater.* **2009**, *8* (1), 47−51.

(7) Koya, A. N.; Zhu, X.; Ohannesian, N.; Yanik, A. A.; Alabastri, A.; Proietti Zaccaria, R.; Krahne, R.; Shih, W.-C.; Garoli, D. Nanoporous Metals: From Plasmonic Properties to Applications in Enhanced Spectroscopy and Photocatalysis. *ACS Nano* **2021**, *15* (4), 6038−6060.

(8) Garoli, D.; Calandrini, E.; Giovannini, G.; Hubarevich, A.; Caligiuri, V.; De Angelis, F. Nanoporous Gold Metamaterials for High Sensitivity Plasmonic Sensing. *Nanoscale Horiz.* **2019**, *4* (5), 1153−1157.

(9) Ding, Y.; Chen, M. Nanoporous Metals for Catalytic and Optical Applications. *MRS Bull.* **2009**, *34* (8), 569−576.

(10) Okulov, I. V.; Weissmüller, J.; Markmann, J. Dealloying-Based Interpenetrating-Phase Nanocomposites Matching the Elastic Behavior of Human Bone. *Sci. Rep.* **2017**, *7* (1), 20.

(11) Balk, T. J.; Eberl, C.; Sun, Y.; Hemker, K. J.; Gianola, D. S. Tensile and Compressive Microspecimen Testing of Bulk Nanoporous Gold. *JOM* **2009**, *61* (12), 26−31.

(12) Ding, Y.; Kim, Y. J.; Erlebacher, J. Nanoporous Gold Leaf: "Ancient Technology"/Advanced Material. *Adv. Mater.* **2004**, *16* (21), 1897−1900.

(13) Coaty, C.; Zhou, H.; Liu, H.; Liu, P. A Scalable Synthesis Pathway to Nanoporous Metal Structures. *ACS Nano* **2018**, *12* (1), 432−440.

(14) Dixon, M. C.; Daniel, T. A.; Hieda, M.; Smilgies, D. M.; Chan, M. H. W.; Allara, D. L. Preparation, Structure, and Optical Properties of Nanoporous Gold Thin Films. *Langmuir* **2007**, *23* (5), 2414−2422.

(15) Pugh, D. V.; Dursun, A.; Corcoran, S. G. Formation of Nanoporous Platinum by Selective Dissolution of Cu from $Cu_{0.75}Pt_{0.25}$. *J. Mater. Res.* **2003**, *18* (1), 216−221.

(16) Wang, X.; Wang, W.; Qi, Z.; Zhao, C.; Ji, H.; Zhang, Z. Electrochemical Catalytic Activities of Nanoporous Palladium Rods for Methanol Electro-Oxidation. *J. Power Sources* **2010**, *195* (19), 6740−6747.

(17) Niauzorau, S.; Kublik, N.; Dasinor, E.; Hasib, A.; Sharstniou, A.; Azeredo, B. Casting of High Surface Area Electrodes Enabled by Low-Temperature Welding of Copper Nanoporous Powders and Nanoparticles Hybrid Feedstocks. *Appl. Mater. Today* **2023**, *32*, 101802.

(18) Fujita, T.; Qian, L.-H.; Inoke, K.; Erlebacher, J.; Chen, M.-W. Three-Dimensional Morphology of Nanoporous Gold. *Appl. Phys. Lett.* **2008**, *92* (25), 251902.

(19) Moschkowitsch, W.; Lori, O.; Elbaz, L. Recent Progress and Viability of PGM-Free Catalysts for Hydrogen Evolution Reaction and Hydrogen Oxidation Reaction. *ACS Catal.* **2022**, *12* (2), 1082−1089.

(20) Yan, K.-L.; Qin, J.-F.; Liu, Z.-Z.; Dong, B.; Chi, J.-Q.; Gao, W.-K.; Lin, J.-H.; Chai, Y.-M.; Liu, C.-G. Organic-Inorganic Hybrids-Directed Ternary NiFeMoS anemone-like nanorods with scaly surface supported on nickel foam for efficient overall water splitting. *Chem. Eng. J.* **2018**, *334*, 922−931.

(21) Ren, Y.; Yang, Y.; Wei, M. Recent Advances on Heterogeneous Non-noble Metal Catalysts toward Selective Hydrogenation Reactions. *ACS Catal.* **2023**, *13* (13), 8902−8924.

(22) Lu, L. Nanoporous Noble Metal-Based Alloys: A Review on Synthesis and Applications to Electrocatalysis and Electrochemical Sensing. *Microchim. Acta* **2019**, *186* (9), 664.

(23) Song, R.; Han, J.; Okugawa, M.; Belosludov, R.; Wada, T.; Jiang, J.; Wei, D.; Kudo, A.; Tian, Y.; Chen, M.; Kato, H. Ultrafine Nanoporous Intermetallic Catalysts by High-Temperature Liquid Metal Dealloying for Electrochemical Hydrogen Production. *Nat. Commun.* **2022**, *13* (1), 5157.

(24) Lee, T.; Corsi, J. S.; Wang, L.; Detsi, E. Air-Stable Nanoporous Aluminum/Lithium Borohydride Fuel Pellets for Onboard Hydrogen Generation by Hydrolysis with Pure Water. *ACS Appl. Energy Mater.* **2021**, *4* (9), 9742−9750.

(25) Corsi, J. S.; Fu, J.; Wang, Z.; Lee, T.; Ng, A. K.; Detsi, E. Hierarchical Bulk Nanoporous Aluminum for On-Site Generation of Hydrogen by Hydrolysis in Pure Water and Combustion of Solid Fuels. *ACS Sustainable Chem. Eng.* **2019**, *7* (13), 11194−11204.

(26) Lee, T.; Fu, J.; Basile, V.; Corsi, J. S.; Wang, Z.; Detsi, E. Activated Alumina as Value-Added Byproduct from the Hydrolysis of Hierarchical Nanoporous Aluminum with Pure Water to Generate hydrogen fuel. *Renewable Energy* **2020**, *155*, 189−196.

(27) Fu, J.; Deng, Z.; Lee, T.; Corsi, J. S.; Wang, Z.; Zhang, D.; Detsi, E. pH-Controlled Dealloying Route to Hierarchical Bulk Nanoporous Zn Derived from Metastable Alloy for Hydrogen Generation by Hydrolysis of Zn in Neutral Water. *ACS Appl. Energy Mater.* **2018**, *1* (7), 3198−3205.

(28) Delahay, P.; Pourbaix, M.; Van Rysselberghe, P. Potential-pH Diagram of Zinc and its Applications to the Study of Zinc Corrosion. *J. Electrochem. Soc.* **1951**, *98* (3), 101.

(29) Murray, J. L. The Al−Zn (Aluminum−Zinc) System. *Bull. Alloy Phase Diagrams* **1983**, *4* (1), 55−73.

(30) Zhou, X.; Darvishi Kamachali, R.; Boyce, B. L.; Clark, B. G.; Raabe, D.; Thompson, G. B. Spinodal Decomposition in Nanocrystalline Alloys. *Acta Mater.* **2021**, *215*, 117054.

(31) Rosenband, V.; Gany, A. Application of Activated Aluminum Powder for Generation of Hydrogen from Water. *Int. J. Hydrogen Energy* **2010**, *35* (20), 10898−10904.
(32) Huang, X.-n.; Lv, C.-j.; Huang, Y.-x.; Liu, S.; Wang, C.; Chen, D. Effects of Amalgam on Hydrogen Generation by Hydrolysis of Aluminum with Water. *Int. J. Hydrogen Energy* **2011**, *36* (23), 15119−15124.
(33) Han, L.-P.; Yao, R.-Q.; Wan, W.-B.; Shi, H.; Wen, Z.; Lang, X.-Y.; Jiang, Q. Hierarchical Nanoporous Intermetallic Compounds with Self-Grown Transition-Metal Hydroxides as Bifunctional Catalysts for the Alkaline Hydrogen Evolution Reaction. *J. Mater. Chem. A* **2019**, *7* (45), 25925−25931.

https://doi.org/10.1021/acsami.4c13394
ACS Appl. Mater. Interfaces 2024, 16, 70469−70476